Construction of Plasmonic Ag and Nitrogen-Doped Graphene Quantum Dots Codecorated Ultrathin Graphitic Carbon Nitride Nanosheet Composites with Enhanced Photocatalytic Activity: Full-Spectrum Response Ability and Mechanism Insight

Yaocheng Deng,[†,‡] Lin Tang,*[,†,‡] Chengyang Feng,[†,‡] Guangming Zeng,*[,†,‡] Jiajia Wang,[†,‡] Yue Lu,[†,‡] Yani Liu,[†,‡] Jiangfang Yu,[†,‡] Song Chen,[†,‡] and Yaoyu Zhou[§]

[†]College of Environmental Science and Engineering and [‡]Key Laboratory of Environmental Biology and Pollution Control, Ministry of Education, Hunan University, Changsha 410082, China

[§]College of Resources and Environment, Hunan Agricultural University, Changsha 410128, China

S Supporting Information

ABSTRACT: The full utilization of solar energy has attracted great attention in the photocatalysis and environmental pollutant control. In this study, the local surface plasmon resonance effect of Ag nanoparticles (Ag NPs) with the upconversion property of nitrogen-doped graphene quantum dots (N-GQDs) was first combined for the formation of ternary Ag/N-GQDs/g-C_3N_4 nanocomposites. The prepared material presents enhanced full-spectrum light response ability, even in near-infrared (NIR) light. The experiment results disclosed that the 0.5% N-GQDs and 2.0% Ag NPs co-doped g-C_3N_4 show the highest photocatalytic activity, achieving 92.8 and 31.3% removal efficiency under full-spectrum light and NIR light irradiation, respectively, which was three-fold than that of pristine g-C_3N_4. The boosted photocatalytic activity can be attributed to the synergistic effect among the g-C_3N_4, N-GQDs, and Ag NPs. The g-C_3N_4 nanosheets can serve as the reaction matrix and support for the dispersion of N-GQDs and Ag NPs, inhibiting their agglomeration. The existence of Ag NPs and N-GQDs can promote the light absorption and transfer ability, leading to the generation of more photoinduced charges. Simultaneously, N-GQDs and Ag NPs can efficiently transfer and reserve electrons, which can accelerate the photoinduced electrons' migration, inhibiting the recombination. The comprehensive effect of the reasons mentioned above resulted in the unique photocatalytic activity of the prepared Ag/N-GQDs/g-C_3N_4 nanocomposites. This study provides a new strategy for the formation of highly efficient photocatalysts with broad-spectrum light response ability and the potential for realistic wastewater pollution control.

KEYWORDS: surface plasmon resonance, upconversion effect, nitrogen-doped graphene quantum dot, tetracycline, full-spectrum light
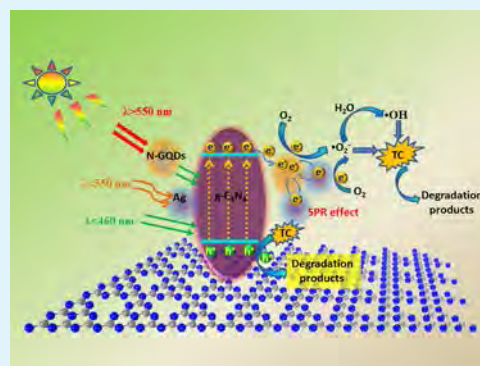
1. INTRODUCTION

In this decade, photocatalysis has been regarded as one of the green and efficient strategies to address both the environmental pollution and energy shortage problems.[1,2] Although the most-studied TiO_2 has admirable photocatalytic activity and chemical stability, the UV-excited intrinsic properties limited its utilization of solar energy and restricted its realistic employment.[3] Therefore, the development of photocatalysts with excellent light response ability not limited to UV-light has become an urgent issue. Recently, many novel semiconductor photocatalysts, such as Cu_2O,[4] $BiVO_4$,[5,6] CdS,[7] and Bi_2WO_6,[8−10] have been designed and demonstrated to be prospective photocatalysts. Among these novel photocatalysts, graphite-like carbon nitride (g-C_3N_4) has attracted great attention.[11−18] Because of the relatively narrow band gap (~2.7 eV), g-C_3N_4 possesses visible-light response ability. Meanwhile, g-C_3N_4 is an environment-friendly, low-cost, easy-

to-obtain, and metal-free polymeric, resulting in its wide application in photocatalytic degradation of environmental pollutants and hydrogen evolution. Moreover, g-C_3N_4 owns the π-conjugated graphene-like porous structure, which ensures unique electron transfer properties and excellent physical−chemical stability.[19,20] However, some demerits cannot be ignored. Although g-C_3N_4 possessed the visible-light response ability, the effective response light was UV−vis light with a wavelength less than 460 nm, which accounts for only a very small proportion of the full-spectrum solar light, resulting in the insensitivity of the broad visible light and near-infrared (NIR) light (~53%) with long wavelength and lower energy. Besides, most of the prepared bulk g-C_3N_4 owns a low specific surface

area (SSA) and high recombination efficiency of photoexcited charges, inhibiting its realistic applications. To solve these problems, exfoliating the bulk into nanosheets and coupling g-C_3N_4 with other materials would be an efficient strategy. Other semiconductors such as Ag_2CrO_4,[14] Cu_2O,[21] Bi_2WO_6,[8,9] CQDs,[22,23] $BiVO_4$[24] have been proved to promote the photogenerated charge transfer and improve the photocatalytic activity. Especially the introduction of quantum dots on the surface of g-C_3N_4 can effectively improve both the charge separation and light utilization efficiency, resulting in boosted photocatalytic performance. Nevertheless, efficient strategies are still needed to improve the photocatalytic activity of g-C_3N_4 in visible light and even in NIR light.

Graphene quantum dots (GQDs), as a new type of QDs, usually present the size of several nanometers and comprise single or few-layer graphene, has attracted great attention in the field of drug delivery, energy conversion, bioimaging, and electrochemical biosensors because of its unique edge effects and quantum confinement.[25−27] Recently, some researchers have found that nitrogen doping was beneficial to improve the optical and electron transfer properties of carbon-based materials and improve its photocatalytic properties. N-GQDs, a special GQD doped with nitrogen atoms, have attracted great attention owing to their low toxicity, excellent electrical conductivity, and photochemistry properties.[28−30] Study results indicated that N-GQDs could efficiently promote the photocatalytic activity of other photocatalysts, which provided a new option for the coupling of N-GQDs with other materials as an advanced material in photocatalysis. Moreover, N-GQDs with upconversion photoluminescence (PL) properties can serve as photosensitizers for capturing visible and NIR light. N-GQDs can also work as electron sink and reservoir in favor of the photogenerated electron migration. However, the photocatalytic performance of single coupled N-GQDs with g-C_3N_4 still needs to improve because most of the upconversion light wavelength of N-GQDs is located at ∼500 nm, which cannot be fully utilized by pristine g-C_3N_4. Therefore, to fully utilize the NIR light and achieve high full-spectrum response ability, it is important to improve the light response in the visible light.

Loading noble-metal nanoparticles (NPs) on the surface was also a promising method to boost the photocatalytic performance of the semiconductors, which can extend visible light absorbed ability for generating more photogenerated electrons and holes by the formed strong electromagnetic field via local surface plasmon resonance (LSPR).[31,32] Meanwhile, the schottky junction formed between noble-metal NPs and semiconductors can also inhibit the recombination of photogenerated charges and retain reduction ability of transferred photoinduced electrons. Among the noble metals, the Ag NP is the cheapest one to own the strongest LSPR effect.[33,34] Recently, coupling of Ag on the g-C_3N_4 surface to synthesize the hybrid composites has aroused great interest.[18,35−38] Although Ag/g-C_3N_4 nanocomposites present enhanced light absorption ability in the whole visible light region, the limited utilization of longer wavelength light, especially for the NIR light, still becomes the bottleneck in their application. Therefore, the co-doping of Ag NPs and N-GQDs on the g-C_3N_4 nanosheet surface would be a promising method.

In this study, we first combined the LSPR effect of Ag NPs, upconversion effect of N-GQDs, and visible light response ability of g-C_3N_4 for the fabrication of novel Ag/N-GQDs/g-C_3N_4 nanocomposites. Under the optimal condition, the prepared Ag/N-GQDs/g-C_3N_4 nanocomposites present en-

hanced tetracycline (TC) removal efficiency compared to pristine g-C_3N_4, reaching 92.8 and 31.3% removal efficiency under full-spectrum light and NIR light irradiation, respectively. The excellent photocatalytic activity of the ternary Ag/N-GQDs/g-C_3N_4 nanocomposites could be attributed to the synergistic effect among the three components. The g-C_3N_4 nanosheets can be treated as the matrix for the loading of Ag NPs and N-GQDs. Ag NPs and N-GQDs can improve the light signal conversion and enhancement effects, which can not only promote the visible light response ability but also convert the long-wavelength light, even NIR light, into visible light, resulting in the efficient utilization of solar energy and the introduction of more photogenerated charges. The existence of Ag NPs and N-GQDs also promote the transfer of the photogenerated charges and reduce its recombination. On the basis of the experimental results obtained in this study, a reasonable mechanism of the prepared Ag/N-GQDs/g-C_3N_4 nanocomposites in this reaction system has been presented.

2. EXPERIMENTAL SECTION

2.1. Materials. Ammonium citrate, melamine, silver nitrate ($AgNO_3$), isopropanol (IPA), triethanolamine (TEOA), and 1,4-benzoquinone (BQ) were purchased from Sinopharm Chemical Reagent Co., Ltd. Other reagents were of analytical grade and used as received without further purification. All solutions were prepared with deionized water (18.25 MΩ cm specific resistance), which was produced by an Ultrapure Laboratory water system.

2.2. Preparation of the Photocatalysts. *2.2.1. Preparation of g-C_3N_4 Nanosheets.* The preparation of g-C_3N_4 nanosheets was synthesized via a two thermal calcination process. Typically, 5 g of dicyandiamide was put into a ceramic crucible with a cover and heated at 550 °C for 4 h in static air with a ramp rate of 2.5 °C/min. After cooling down to room temperature, the obtained yellow agglomerates were milled into powder. Then, 1 g of the bulk g-C_3N_4 obtained as mentioned above was placed in a ceramic crucible without a cover and heated at 500 °C for 2 h with a ramp rate of 5 °C/min. The ultimately obtained light yellow powder was the g-C_3N_4 nanosheets.

2.2.2. Preparation of N-GQDs. The N-GQDs were obtained by an easy reflux method under the atmospheric pressure. In detail, 2.0 g of $C_6H_5O_7(NH_4)_3$ was first dissolved into 40 mL of H_2O and then put into a flask that was equipped with a condenser tube and followed by heating the reaction system to 200 °C with an oil bath pan. After about 0.5 h, the color of the liquid became orange, indicating the formation of N-GQDs. Next, the pH of the obtained aqueous solution was adjusted to 7.0 by the addition of NaOH solution (10 mg/mL). Finally, solid N-GQDs were obtained by freeze-drying the solution.

2.2.3. Preparation of N-GQDs/g-C_3N_4 Nanosheet Composites. The N-GQDs/g-C_3N_4 nanosheet composites were synthesized as follows. First, an appropriate amount of g-C_3N_4 nanosheets was dispersed in 60 mL of ethanol and sonicated for 60 min to obtain a homogeneous suspension. Then, a certain amount of N-GQDs was added into the above-mentioned homogeneous solution and kept stirring for 24 h. Next, the ethanol was vaporized completely, and the obtained solid sample was further dried at 80 °C. Then, the prepared sample was washed with water several times and dried. A series of N-GQDs/g-C_3N_4 composites with different N-GQD contents were prepared by adjusting the added dosage of N-GQDs. The prepared N-GQDs/g-C_3N_4 composites were designed as GCN-X (X = 1, 2, 3, 4, 5), wherein "*X*" represents the mass ration of N-GQDs in the hybrid composite of 0.1, 0.3, 0.5, 0.7, and 1.0%, respectively.

2.2.4. Preparation of Ag/N-GQDs/g-C_3N_4 Composites. The prepared process of Ag/N-GQDs/g-C_3N_4 composites was achieved via a photoreduction procedure. Typically, an appropriate amount of $AgNO_3$ and the 0.5% N-GQDs/g-C_3N_4 (GCN-3) were added to 20 mL of methanol aqueous solution (containing 4 mL methanol) in a beaker. The suspension was stirred under the irradiation of a UV lamp for 30 min. After that, the suspension was collected by filtration and thoroughly washed with ethanol and deionized water several times to

remove the residual impurity, and then, the sample was dried at 60 °C in a vacuum oven for 12 h. The prepared samples were marked as AGCN-Y. (Y presents the mass ratio of Ag to the samples, and Y = 1, 2, 3, 4, and 5 represent 0.5, 1.0, 1.5, 2.0, and 2.5%, respectively). For comparison, 2.0% Ag/g-C_3N_4 (abbreviated as Ag/g-C_3N_4 in the following text) was also prepared via the same procedure using pristine g-C_3N_4 nanosheets.

2.3. Characterization of Materials. The crystal structure characteristics of the prepared samples were measured via an X-ray diffractometer (XRD) (Bruker AXS D8 ADVANCE) with a Cu Kα irradiation source at a scan rate (2θ) of 0.05° s^{-1}. Morphology analysis was based on transmission electron microscopy (TEM) and high-resolution TEM, which was obtained via an F20 S-TWIN electron microscope (Tecnai G2, FEI Co.) at an acceleration voltage of 200 kV. The SSAs of the prepared samples were characterized via a nitrogen adsorption−desorption and Brunauer−Emmett−Teller (BET) method by a surface area analyzer (NOVA 2200e, Quantachrome). FT-IR spectra were obtained on an IRAffinity-1 Fourier transform infrared (FTIR) spectrometer (Shimadzu, Japan) at room temperature by the standard KBr disk method. The X-ray photoelectron spectroscopy of the prepared samples was carried out by a Thermo Fisher ESCALAB 250Xi spectrometer with an Al Kα source. The ultraviolet−visible NIR diffused reflectance spectra (UV−vis−NIR DRS) of the prepared samples were recorded via a UV−vis−NIR spectrophotometer (Hitachi U4100 UV spectrometer) equipped with an integrating sphere, using BaSO$_4$ as the reference. The PL spectra were studied through an F-7000 fluorescence spectrometer. The electron spin resonance (ESR) signals of radicals spin-trapped by the spin-trapped reagent 5,5-dimethyl-L-pyrroline N-oxide (DMPO) were measured on a Bruker ER200-SRC spectrometer under visible light irradiation (λ > 420 nm).

2.4. Photocatalytic Activity Measurement. The photocatalytic activity of the prepared photocatalysts was investigated by the degradation of TC under light irradiation. The light source was a 300 W Xe lamp (PLS/SXE 300C, Beijing Perfectlight Co., Ltd.). The Xe lamp was equipped with a UV cutoff filter to remove the light at a wavelength less than 420 nm as the visible light source, a 760 nm filter as the NIR light source, and no filter as the full-spectrum light source. The spectra irradiance distribution of the light sources is presented in Figure S1, and the average photon flux density was 3.15 einstein·L^{-1}·S^{-1} under full-spectra light (λ > 365 nm), 2.89 × 10^{-5} einstein·L^{-1}·S^{-1} under visible light (λ > 420 nm), and 0.48 × 10^{-5} einstein·L^{-1}·S^{-1} under NIR light (λ > 760 nm). The photocatalytic reaction system is shown in Figure S2. Before the photocatalytic experiments start, 20 mg of the as-prepared photocatalysts was added into 100 mL of 20 mg/L TC aqueous solution and kept stirring in the dark for 30 min to achieve the adsorption equilibrium. During the illumination process, quantitative aqueous solution was collected at certain time intervals for analysis after centrifugation to remove the photocatalyst. The photocatalytic degadation efficiency was measured using a Shimadzu UV−vis spectrophotometer (UV-2550) at the characteristic absorption peak of 357 nm for TC.

2.5. Photoelectrochemical Measurement. The photoelectro-chemical characteristics of the prepared samples were measured by a typical three-electrode measured system based on a CHI 660D workstation. A Pt electrode was used as the counter electrode, and an Ag/AgCl electrode in saturated KCl solution was employed as the reference electrode. The photoelectrochemical test system was conducted in a 0.2 M sodium sulfate electrolyte solution under visible light provided by a 300 W Xe arc lamp with a UV cutoff filter (λ > 420 nm). The photocurrent density and electrochemical impedance spectroscopy (EIS) measurements were carried out based on the above-mentioned photoelectrochemical test system.

3. RESULTS AND DISCUSSION

3.1. Crystal Structure and Morphology Analysis. The XRD analysis was carried out to identify and determine the different phase structures of the synthesized samples. As shown in Figure 1, for pristine g-C_3N_4, one obvious peak located at
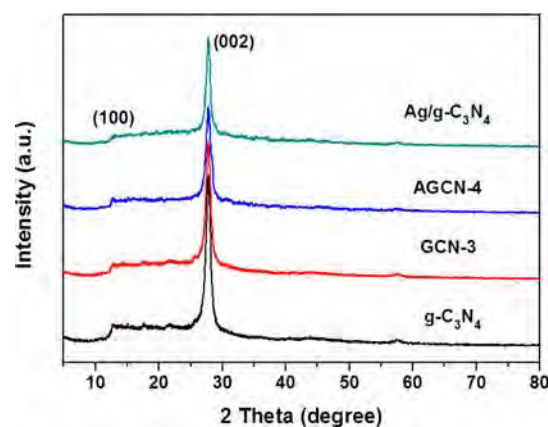

Figure 1. XRD patterns of the prepared g-C_3N_4, GCN-3, Ag/g-C_3N_4, and AGCN-4.

27.4° can be clearly observed, which represents the (002) characteristic crystal plane of g-C_3N_4. Another relatively weak peak at 13.0° refers to the (100) crystal plane of g-C_3N_4. The existence of the two characteristic peaks indicated the characteristic graphitic-like layered stacking of CN-based materials.[13,14,39] Nevertheless, as for the GCN-3 and Ag NPs co-doped g-C_3N_4 (AGCN-4) samples, no characteristic peaks belonging to N-GQDs can be found owing to their high dispersion and low content.[40] In addition, because of similar reasons, the characteristic peak of Ag also cannot be found. Besides, all the other three samples obtained the characteristic peaks of pristine g-C_3N_4, indicating that the coating of N-GQDs and Ag NPs cannot disturb the crystal structure of g-C_3N_4, which is important for the high performance of the prepared hybrid composites. Additionally, it can be seen that when the N-GQDs or the Ag NPs are loaded on g-C_3N_4, the relative intensity of the (002) peak in these samples decreases. This phenomenon could be attributed to the fact that the N-GQDs and Ag NPs did not only cover the shallow surface of g-C_3N_4 but also entered between different g-C_3N_4 layers, presenting the adjusted distance of layers.[41]

To study the morphology and the structure of the prepared samples, TEM and HR-TEM images are provided in Figure 2. From Figure 2a,b, the prepared N-GQDs display the monodispersed qusi-spherical shape, possess the lattice spacing of 0.200 nm, and are mainly distributed in 3−7 nm with the average diameter of 5 nm (Figure 2c), indicating the successful preparation of N-GQDs.[28] The morphology of the prepared GCN-3 was also investigated by TEM (Figure 2d−f), in which some dense dark spots were distributed uniformly on the surface of g-C_3N_4 nanosheets with a lattice distance of 0.200 nm, indicating the existence of N-GQDs. The other region shows the amorphous forms referring to g-C_3N_4 nanosheets. As for AGCN-4 samples, the nanosheet structure of g-C_3N_4 can be clearly observed, and similar to GCN-3, some dense dark spots are dispersed homogeneously. Additionally, in the HR-TEM of the AGCN-4 sample, another new crystal with the lattice distance of 0.237 nm can be found, which belongs to the (111) crystalline of metallic Ag[42] (Figure 2g−i). This result indicates the co-existence of N-GQDs and Ag NPs on the g-C_3N_4 nanosheet surface and the successful preparation of as-designed Ag/NGQDs/g-C_3N_4 composites. Besides, the Ag NPs and N-GQDs firmly rely on each other and intimately contact with g-C_3N_4, providing persuasive evidence for the formation of heterostructures. This phenomenon indicates that in the
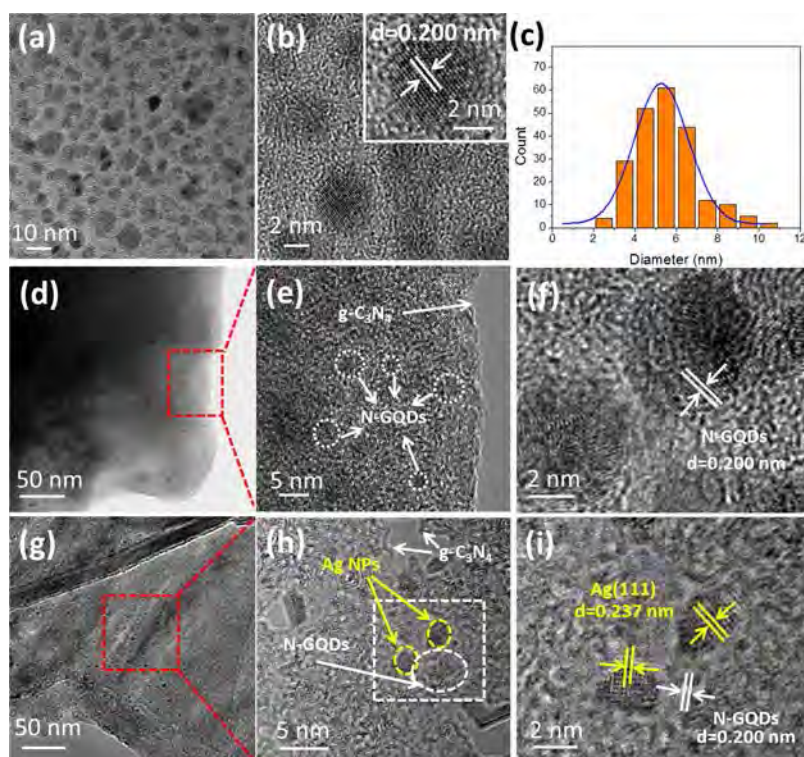
Figure 2. (a) TEM and (b) HRTEM images of N-GQDs, and (c) corresponding particle size distribution of N-GQDs; (d−f) TEM and HRTEM of GCN-3; and (g−i) TEM and HRTEM images of AGCN-4.
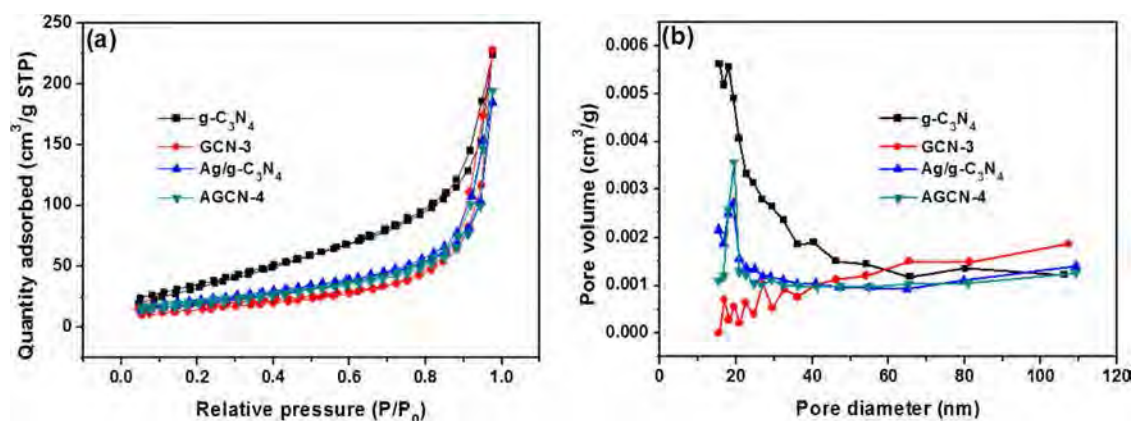

Figure 3. (a) N_2 adsorption−desorption spectra of prepared $g-C_3N_4$, GCN-3, $Ag/g-C_3N_4$, and AGCN-4, and (b) corresponding pore size distribution.

deposition process of Ag NPs, the photogenerated electrons tend to transport and accumulate on the surface of N-GQDs and are received by Ag^+ for the formation of Ag. The unique structure was beneficial to the transportation of electrons and holes, which can decrease the recombination rate of photo-generated charges, leading to high photocatalytic activity and degradation performance.

3.2. SSA and Pore Size Distribution Analysis. To investigate the SSAs and pore volume of the samples, the nitrogen adsorption−desorption isotherms of the as-prepared composites are presented in Figure 3. The relative BET SSA and pore volume of the samples are shown in Table 1. It can be seen that the isotherms of the as-prepared sample exhibit a classical type IV isotherm, combined with the pore size distribution spectra disclosed in Figure 3b, indicating the presence of a mesoporous structure.[14] The SSA of pristine g-

Table 1. SSA and Pore Volume of the As-Prepared Photocatalysts

samples	SSA (m^2/g)	pore volume (cm^3/g)
$g-C_3N_4$	123.25	0.34
GCN-3	64.99	0.35
AGCN-4	76.67	0.31
$Ag/g-C_3N_4$	70.73	0.29

C_3N_4 nanosheets is 123.25 m^2/g, which is larger than the other three samples, and the pore volume is 0.34 cm^3/g. The prepared GCN-3 sample owns an SSA of 64.99 m^2/g, which is less than that of pristine $g-C_3N_4$ nanosheets. However, despite that, GCN-3 owns a low SSA, and its pore volume is 0.35 cm^3/g, which is a little larger than that of pristine $g-C_3N_4$ nanosheets. This phenomenon results from the fact that the

loading of N-GQDs on the g-C$_3$N$_4$ nanosheet surface would lead to the decrease of the SSA. However, N-GQDs not only covered the g-C$_3$N$_4$ nanosheet surface but were also coupled to different g-C$_3$N$_4$ layers because of their small size, leading to in-depth shaving even severing of the thinner nanolayer on GCN-3, generating more volume to expose. This result was also consistent with the analysis in XRD results. After the coating of Ag on the surface of GCN-3 for the formation of AGCN-4, the SSA of AGCN-4 increased from 64.99 to 76.67 m^2/g, but the pore volume decreased from 0.35 to 0.31 cm^3/g. The coating of Ag on the surface of GCN-3 would further improve the surface roughness of the sample, which resulted in the increase of the SSA, and the additional Ag NPs would occupy the volume expanded by the N-GQDs among the g-C$_3$N$_4$ layers, so the volume decreased to some extent.[41] The proper SSA and porous architecture can provide more active sites for contaminant molecular absorption and migration of products, contributing to high photocatalytic activity and degradation performance.

3.3. Surface Chemical Composition Analysis. To investigate the structure variation after the coating of N-GQDs and Ag NPs, the FT-IR spectra of the as-prepared samples are provided. As shown in Figure 4, the pristine g-C$_3$N$_4$
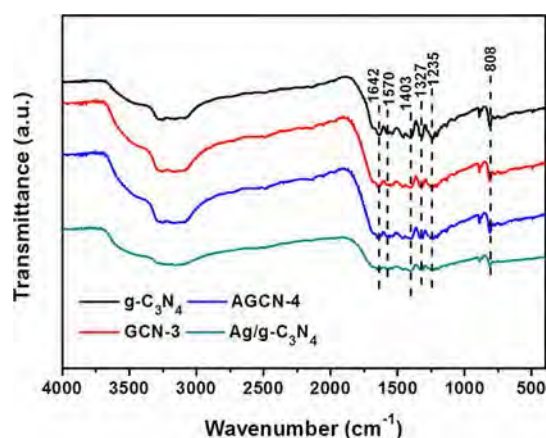
Figure 4. FTIR spectra of the prepared g-C$_3$N$_4$, GCN-3, Ag/g-C$_3$N$_4$, and AGCN-4 samples.

presents the typical FT-IR spectra. The peak in 808 cm^{-1} refers to the unique breathing mode for triazine rings of g-C$_3$N$_4$. The peak located in the region of 1200−1650 cm^{-1} is attributed to stretching vibration modes of C−N and C≡N hetero-cycles.[43,44] The peaks from 3000 to 3600 cm^{-1} belong to N−H groups, which originate from the uncondensed amino groups or the residual hydrogen atoms bound to the edges of the graphite-like CN.[45] It should be noted that the characteristic peak at 1270 cm^{-1} referring to the C−OH of N-GQDs cannot be detected in GCN-3 and AGCN-4 samples, which is mainly because of the strong stretching vibration of C−N and the low loading amount of N-GQDs.[40] According to the aforementioned analysis, the surface chemical structures of g-C$_3$N$_4$ are retained in the coating of N-GQDs and Ag NPs, which is essential to the enhanced photocatalytic activity.

To further study the chemical states of the samples and to analyze the intimate interaction between N-GQDs, Ag, and g-C$_3$N$_4$, XPS spectra and element content of pristine g-C$_3$N$_4$, GCN-3, and AGCN-4 were surveyed in Figure 5a and Table S1, indicating the presence of carbon, nitrogen, oxygen, whereas silver only exists in the AGCN-4 sample. Figure 5b

shows the high-resolution C 1s spectra of the three prepared samples; like pristine g-C$_3$N$_4$, the main peak located at 287.9 eV can be attributed to the sp^2-hybridized carbon in an N-containing aromatic ring (N−C≡N).[43] However, for GCN-3 and AGCN-4 samples, more peaks can be divided. The peak at 284.6 eV refers to C−C bonds, and another peak at 285.2 eV can be assigned to C−N bonds. The peak at 286.1 eV is assigned to C−O, and 289.3 eV belongs to O−C≡O of N-GQDs, demonstrating the co-existence of N-GQDs and g-C$_3$N$_4$ in the composites.[28,46,47] Figure 5c discloses the high-resolution N 1s spectrum with three main species peaks for all the samples at 398.4, 400.4, and 404.1 eV. The signal peak at 398.4 eV binding energy is attributed to electrons originated from sp2-hybridized nitrogen atoms in C−N≡C. The peak located at 400.4 eV belongs to the tertiary nitrogen (N−(C)$_3$), and the peak at 404.1 eV originates from the charging effects of the positive charge location.[13,43] As for GCN-3 and AGCN-4 samples, another small peak located at 401.3 eV can be found, which refers to the N−H, indicating the successful synthesis of N-GQDs.[28,47,48] From the high-resolution XPS spectrum of O 1s, the peaks of pristine g-C$_3$N$_4$ were very weak though oxygen could be coupled into this composite because of the calcination process for the formation of g-C$_3$N$_4$ nanosheets. For GCN-3 and AGCN-4, the major peak centered at 531.5 eV corresponds to O−C/O−H bonds, whereas the binding energy at 532.8 eV belongs to C≡O, both of which can be ascribed to the oxygenic components of N-GQDs.[47,48] As for the high-resolution spectra of Ag 3d, it can be seen that for pristine g-C$_3$N$_4$ and GCN-3, there is no clear peak of Ag, indicating no Ag element in the sample. However, for AGCN-4, the strong shaken-up satellite doublets of Ag 3d with binding energies of 368.1 and 374.1 eV are identified as Ag 3d$_{5/2}$ and Ag 3d$_{3/2}$ orbitals attributed to metallic Ag, which indicates the formation of Ag NPs in the AGCN-4 sample.[33,49] The aforementioned results indicate that the formation of Ag and N-GQDs on the Ag/N-GQDs/g-C$_3$N$_4$ composites is successful, and the introduction of silver and N-GQDs has little influence on the chemical modification of the g-C$_3$N$_4$ template.

3.4. Photocatalytic Degradation Experiments. *3.4.1. The Influence of N-GQDs and Ag Content.* The coating content of N-GQDs and Ag would make a great effect on the photocatalytic activity of the prepared Ag/N-GQDs/g-C$_3$N$_4$. We carried out a series of experiments to investigate the optimal coating content of N-GQDs and Ag for the removal of TC under visible light irradiation ($\lambda > 420$ nm). The relative description and data are presented in the Supporting Information (Figure S3). On the one hand, the attachment of N-GQDs on the g-C$_3$N$_4$ surface can absorb more light energy and increase the light utilization efficiency. On the other hand, the heterojunction formation between N-GQDs and g-C$_3$N$_4$ can be achieved, which can inhibit the recombination efficiency of photogenerated charges and transfer the photogenerated charges to the reaction sites of the photocatalysts. However, an excessive amount of N-GQDs tend to act as a recombination center and weaken the function of N-GQDs for light absorption and electron pathways, and then, the recombination rate of photogenerated charges will increase. Similarly, the proper coating amount of metallic Ag enhances the light absorption ability and serves as an electron sink to accelerate the electron migration efficiency. However, excess metallic Ag will become the recombination center, resulting in the decreased photocatalytic performance.[50] The results indicated that the 0.5% N-GQDs and 2.0% AGCN-4 show the highest
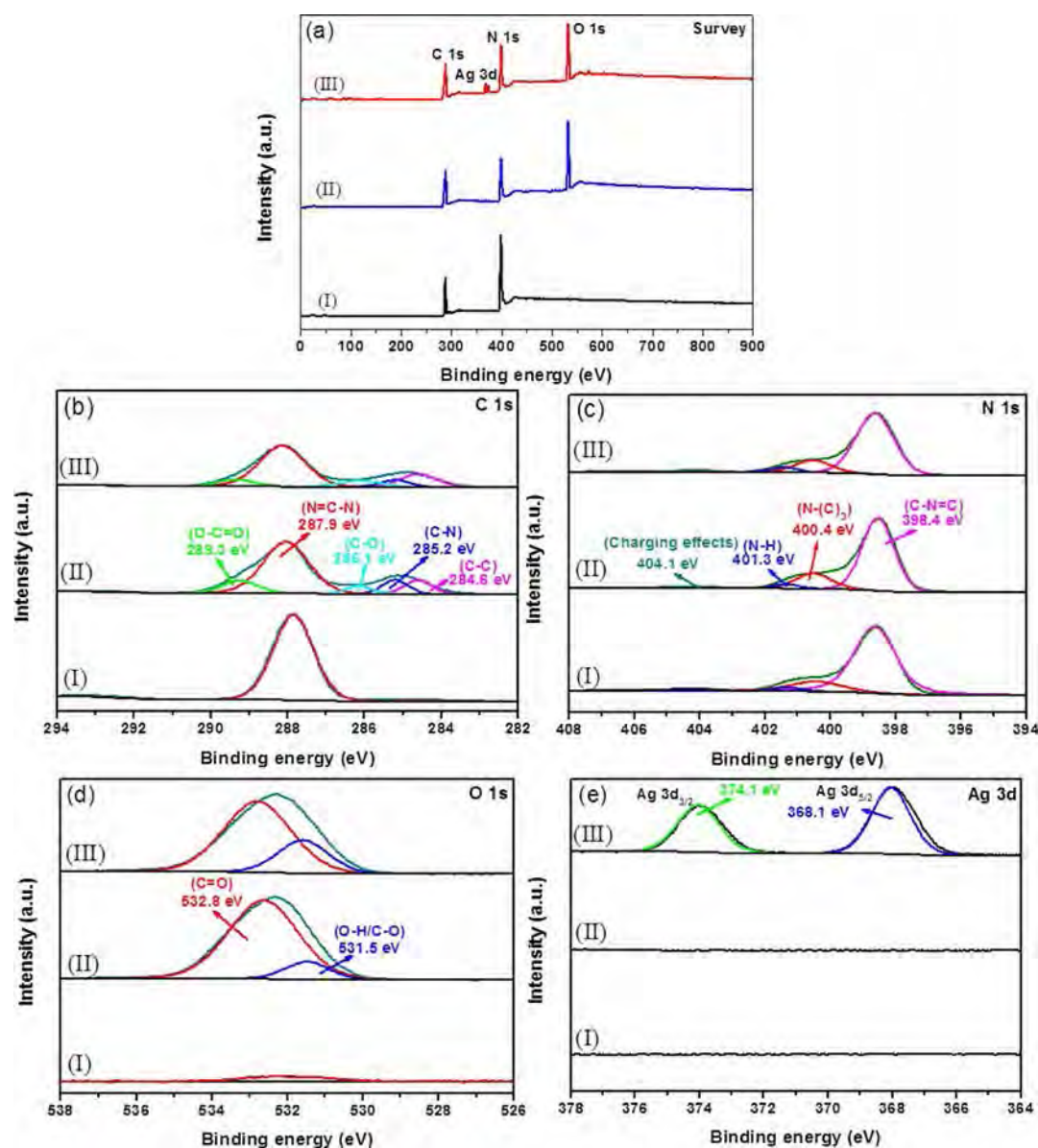
Figure 5. XPS spectra of the as-synthesized samples: (a) survey spectra and (b−e) high resolution of C 1s, N 1s, O 1s, and Ag 3d, respectively. (I) g-C$_3$N$_4$, (II) GCN-3, and (III) AGCN-4.

photocatalytic activity, presenting a 90.11% of TC degradation efficiency. Further increasing the contents of Ag and N-GQDs would lead to the decreased degradation efficiency of TC.

3.4.2. The Influence of Different Light Irradiation Condition. The full utilization of solar energy has become one of the research hotspots in the photocatalytic field to both achieve environmental remediation and avoid secondary pollution. Thus, to fully evaluate the photocatalytic performance of the as-prepared photocatalysts, the photocatalytic degradation experiments for TC removal have been conducted under a xenon lamp without any filter ($\lambda > 365$ nm) or with an NIR-cut optical filter ($\lambda > 760$ nm) to simulate the degradation experiments in the whole spectrum or in the NIR light, and the results are presented in Figure 6. As shown in Figure 6a−c, under the full-spectrum light irradiation ($\lambda > 365$ nm), all the samples present boosted photocatalytic activity for TC removal, and the optimum samples (AGCN-4) showed a 92.8% removal efficiency with a k value of 0.0428 min^{-1}, which was higher than that under visible light irradiation ($\lambda > 420$ nm). This

phenomenon could be explained by the fact that shorter wavelength of the light indicates greater energy of its photon processes. Therefore, under the irradiation of full spectrum, more light energy can be employed, so the photocatalytic performance can be further improved.

As we all know, the NIR light takes account of a great part of solar light, and because of the existence of the upconversion effect of N-GQDs and the LSPR effect of metallic Ag, we also investigated the NIR light response ability of different photocatalysts for TC removal under NIR light irradiation ($\lambda > 760$ nm). From Figure 6d, we can see that, because of the long wavelength and the relatively weak energy of NIR light, it is inevitable that the photocatalytic activity declines greatly under NIR light irradiation compared with those under visible light or full-spectrum light. Besides, owing to the poor NIR light response ability, pristine g-C$_3$N$_4$ presented the weakest photocatalytic performance. The prepared GCN-3 and Ag/g-C$_3$N$_4$ sample show enhanced photocatalytic performance than pristine g-C$_3$N$_4$ under NIR light irradiation because of the
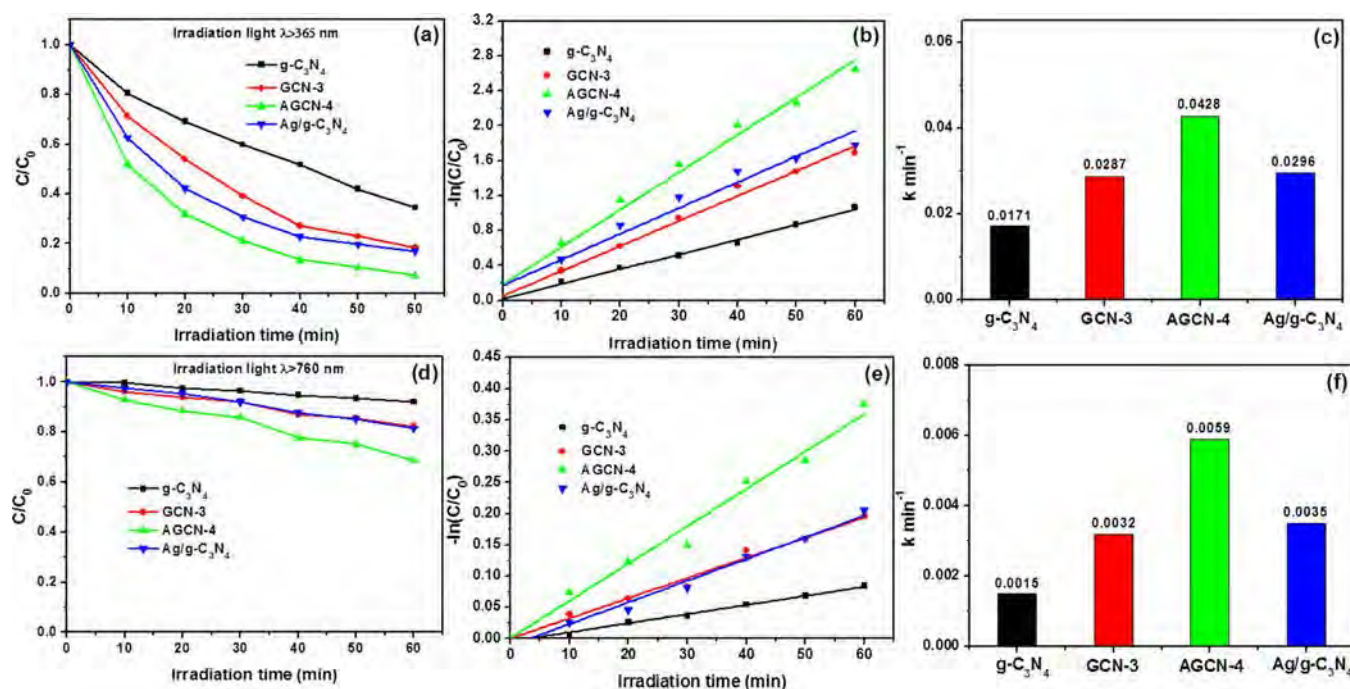
Figure 6. Photocatalytic degradation process with different photocatalysts (a) under full-spectrum light irradiation (λ > 365 nm) and the (b,c) relative reaction dynamic data and (d) under NIR light irradiation (λ > 760 nm) and the (e,f) relative reaction dynamic data.
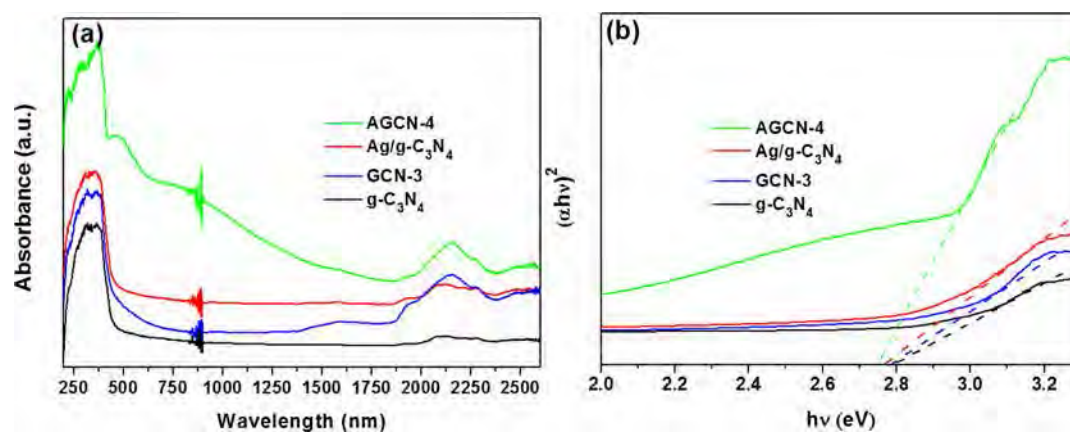

Figure 7. (a) Optical ability of the prepared g-C_3N_4, GCN-3, Ag/g-C_3N_4, and AGCN-4 and (b) corresponding band gap value.

upconversion effect of N-GQDs or the LSPR effect of metallic Ag. In this case, the photocatalytic activity of the prepared binary GCN-3 or Ag/g-C_3N_4 is still very low because in the NIR light region, g-C_3N_4 cannot be efficiently excited, and the migration of photogenerated charges in g-C_3N_4 is inhibited greatly. Besides, the wavelength of the converted light is mainly located on 500 nm, which cannot be fully utilized by g-C_3N_4.[51,52] It is interesting that the photocatalytic activity of the N-GQDs and Ag co-doped g-C_3N_4 ternary nanocomposites is further improved, presenting a 31.3% removal efficiency and 0.0059 min^{-1} reaction rate (Figure 6e,f). The boosted photocatalytic activity is mainly due to the synergistic effect of the upconversion and LSPR effects of N-GQDs and metallic Ag NPs. Because of the existence of N-GQDs, long wavelength can be absorbed and converted into shorter-wavelength light and employed by the metallic Ag to enhance its LSPR effect, resulting in more photogenerated electrons and holes. Meanwhile, the existence of N-GQDs and metallic Ag can accelerate the transfer of photogenerated charges and inhibit their recombination efficiency. Therefore, more photogenerated charges can attend the degradation process and bring about improved photocatalytic performance.

3.5. Optical Properties. The optical properties of the obtained samples were studied by UV−vis−NIR DRS at room temperature. As shown in Figure 7a, the pristine g-C_3N_4 nanosheets have an absorption edge at around 460 nm. As for GCN-3, because of the existence of N-GQDs, the light absorption ability was enhanced in the whole visible light region, even to the NIR light region, because of the strong absorption ability of the visible light and the upconversion ability to change NIR light to visible light. As for Ag/g-C_3N_4 composites, enhanced light absorption ability can also be found, which could be owing to the intense LSPR of nanostructured silver. It is amazing to notice that the greatly enhanced light absorption ability appears on the AGCN-4 composites with the coupling of Ag and N-GQDs, from the visible light to NIR light region. It is interesting that there are characteristic peaks in the range of 450−550 nm because of the LSPR effect of metallic
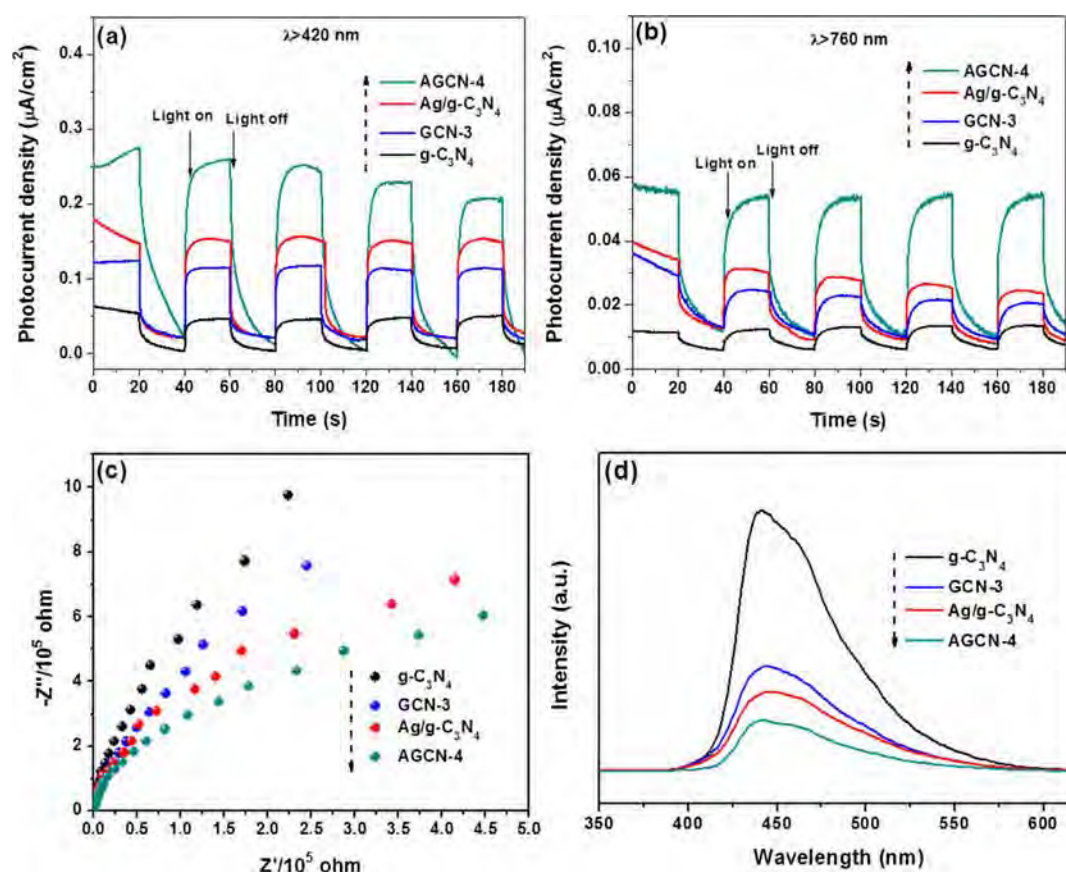
Figure 8. Transient photocurrent responses of g-C$_3$N$_4$, GCN-3, Ag/g-C$_3$N$_4$, and AGCN-4 (a) under visible light irradiation and (b) NIR light irradiation and (c) EIS Nyquist plots and (d) PL spectra of g-C$_3$N$_4$, GCN-3, Ag/g-C$_3$N$_4$, and AGCN-4 samples.

silver.[53,54] However, this characteristic peak cannot be found in Ag/g-C$_3$N$_4$ samples with the same Ag content. This phenomenon could be explained by the synergistic effect between N-GQDs and Ag NPs. The up–conversion properties of N-GQDs can change the light from NIR to visible light to be further utilized by Ag at round 500 nm and then enhance the LSPR effect of Ag NPs. That is the reason why there are characteristic peaks for the LSPR effect of Ag in AGCN-4 but not in Ag/g-C$_3$N$_4$. This result also further demonstrated that coupling N-GQDs and Ag can greatly improve the photocatalytic performance of the hybrid composites. It is well-known that the change of light absorption ability indicates the change of the band gap, so the corresponding direct band gaps of the semiconductors are calculated by converted $(ah\nu)^2$ versus $h\nu$, where a, h, and ν represent the absorption coefficient, Planck constant, and optical frequency, respectively.[13,14] Herein, the band gap of the prepared g-C$_3$N$_4$, GCN-3, Ag/g-C$_3$N$_4$, and AGCN-4 are 2.79, 2.77, 2.76, and 2.74 eV, respectively (Figure 7b). The band gap of AGCN-4 has shrunk from 2.79 to 2.74 eV, which may be suitable for absorbing more visible light, even NIR light, to improve the photocatalytic activity and photodegradation performance. The unique optical property of the prepared Ag/N-GQDs/g-C$_3$N$_4$ hybrid system has presented its great potential to become a full-spectrum response photocatalytic material.

3.6. Photoelectrochemical and PL Analysis. To investigate the charge transfer and separation conditions of pristine g-C$_3$N$_4$, GCN-3, Ag/g-C$_3$N$_4$, and AGCN-4, the relative transient photocurrent response, EIS Nyquist plots, and PL spectra were provided. Figure 8a presents the transient photocurrent response ability of the sample under visible light with light on–off cycles ($\lambda > 420$ nm). It is clear to see that the photocurrent density of all the samples increases instantaneously and keeps at a relative constant value. It is noticeable that the pristine g-C$_3$N$_4$ presents the lowest photocurrent density, and the GCN-3 displays relatively higher photocurrent density, which is attributed to the enhanced light response ability and promoted photogenerated charge generation and transfer rate for the existence of N-GQDs. The as-prepared Ag/g-C$_3$N$_4$ also shows higher photocurrent density than pristine g-C$_3$N$_4$, owing to the LSPR effect and excellent electron transportation ability of metallic Ag. The highest photocurrent density belongs to the AGCN-4 sample, which is about fivefold as much as that of pristine g-C$_3$N$_4$, demonstrating the synergistic effect of Ag NPs and N-GQDs in more efficient separation of photogenerated electron–hole pairs to minimize the recombination, which coincides with the results of the photocatalytic activity measurements. Additionally, the photocurrent density of different photocatalysts under NIR light irradiation also has been investigated (Figure 8b). It can be seen that pristine g-C$_3$N$_4$ presents very little photocurrent density, and the prepared AGCN-4 shows the highest photocurrent density, nearly sixfold than pristine g-C$_3$N$_4$, indicating the promoted photocatalytic performance of the prepared AGCN-4 because of the existence of N-GQDs and Ag NPs. The results are also consistent with the photocatalytic degradation performance in Figure 6.

EIS Nyquist plots also provide another corroborative evidence for studying interfacial charge transfer behaviors of pristine g-C$_3$N$_4$, GCN-3, Ag/g-C$_3$N$_4$, and AGCN-4 photo-

electrodes. It is well-known that the smaller diameter indicates the weaker impedance and more efficient charge transfer. In Figure 8c, the AGCN-4 sample presents the smallest diameter among the samples, indicating the best electronic conductivity because the tight interface connection accomplished by the addition of N-GQDs and Ag NPs promotes the interfacial charge transfer and the photocatalytic performance.

PL spectra were provided as another characterization method to investigate the migration and separation circumstance of photogenerated charges. In Figure 8d, the similar broad emission band centered in the range of 440−500 nm appears for all the samples with an excitation wavelength set at 320 nm. As can be clearly seen, compared with the highest PL peaks of pristine $g-C_3N_4$, the emission intensity of GCN-3 substantially decreases, indicating the recombination process of the photogenerated charges is efficiently suppressed after an appropriate amount of N-GQD modification. Moreover, the intensity of $Ag/g-C_3N_4$ is comparatively lower than the former two, demonstrating that the photoelectrons are ulteriorly transferred via the interface to accelerate the carrier separation by modified Ag NPs. Among the four samples, the prepared AGCN-4 sample presents the lowest PL intensity, which indicates an excellent electron separation rate and transportation efficiency. To demonstrate the upconversion property of the prepared N-GQDs directly, the upconverted PL spectra of N-GQDs have been measured. As shown in Figure S4, it can be seen that when the prepared N-GQDs were excited at 500−1000 nm, the emissions were located at visible light wavelengths (450−600 nm). In other words, N-GQDs own obvious upconverted property and can absorb long wavelength light (NIR light) and convert to short wavelength light (450−600 nm), which can in turn excite the visible-light induced photocatalysts to produce photogenerated electron−hole pairs, promoting the light absorbing ability of the photocatalysts and improving the corresponding photocatalytic activity. This is why the prepared $Ag/N-GQDs/g-C_3N_4$ ternary nanocomposites show the unique photocatalytic activity and degradation performance. The synergistic effect between Ag NPs and N-GQDs guarantees the enhanced photocatalytic activity.

3.7. Stability of the As-Prepared $Ag/N-GQDs/g-C_3N_4$ Nanocomposites. Taking the realistic applications into consideration, the recycle experiment of the prepared $Ag/N-GQDs/g-C_3N_4$ (AGCN-4) nanocomposites has been conducted. As shown in Figure 9, after five repeated photocatalytic experiments, the photocatalytic removal efficiency of TC by AGCN-4 still reaches 85.5%, which indicates the high stability and good performance of the photocatalyst. Besides, to further study the structure and chemical stability of the photocatalyst, the XRD and FTIR analysis of the samples before and after the photocatalytic reaction are provided to make comparison. As shown in Figures 10a and 11b, the XRD pattern and FTIR spectra of the used AGCN-4 nanocomposites nearly stay the same as those of fresh samples. The results demonstrated the excellent stability of the prepared $Ag/NGQDs/g-C_3N_4$ nanocomposites.

3.8. Possible Photocatalytic Reaction Mechanism. To investigate the reaction process and the electron transfer mechanism in this reaction system, the roles of three common active oxidant species, hydroxyl radical (•OH), hole (h⁺), and superoxide radical (•O_2^-), have been studied. Herein, IPA, TEOA, and BQ were used as the scavengers for •OH, h⁺, and •O_2^-, respectively.[55] The addition dosage of these scavengers was 1 mM, and the results are presented in Figure 11a,b. When
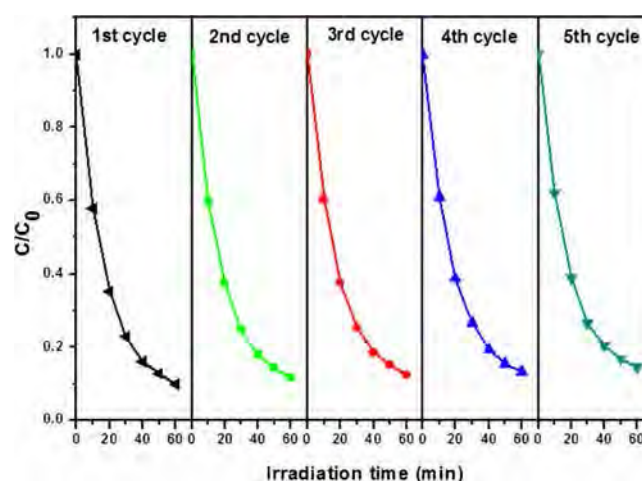

Figure 9. Recycle experiments of AGCN-4 nanocomposites for the photocatalytic degradation of TC under visible light irradiation.

these scavengers were added into the photocatalytic degradation system, the photocatalytic removal efficiency was inhibited in various degrees, indicating that all the three species participated in the photocatalytic degradation process. As for IPA, when it was added into the reaction system, the removal efficiency of TC decreased from 90.11 to 69.21%, indicating that IPA played an important role in the TC removal process. When TEOA was added, the removal efficiency of TC experienced a sharp decrease from 90.11 to 33.12%, indicating that the h⁺ species were the major reaction species for TC degradation. Meanwhile, in the presence of BQ, the degradation efficiency was also inhibited, implying that •O_2^- radical species also played a vital role in the photocatalytic degradation process. Additionally, to further verify the role of •O_2^- radical species, a photocatalytic experiment under an N_2 ambient condition was conducted. Similarly, the decreased TC degradation efficiency under an N_2 ambient condition indicates that the dissolved oxygen also influenced the reaction process by reacting with the produced photogenerated electron to generate •O_2^- radical species. On the basis of these results, it is clear to conclude that h⁺ played a major role in the TC degradation in the reaction system, and •O_2^- and •OH also influenced the removal efficiency greatly.

To further definitely affirm the generation of •O_2^- and •OH species, the ESR spin-trap measurement based on $g-C_3N_4$ and $Ag/N-GQDs/g-C_3N_4$ photocatalysts under visible light irradiation was conducted. The experiments were carried out both under dark and visible light irradiation conditions. As shown in Figure 12a,b, under the irradiation of visible light, some characteristic peaks of DMPO−•O_2^- are observed for $g-C_3N_4$ and AGCN-4 nanocomposites, and the peak intensity of AGCN-4 is higher than pristine $g-C_3N_4$, indicating that more •O_2^- radical species were generated in the AGCN-4-based reaction system. However, no signals appear under dark conditions. Similarly, DMPO−•OH adducts with four characteristic peaks with a 1:2:2:1 intensity pattern are also observed for these two composites under visible light irradiation, and the peak intensity of AGCN-4 is also higher than pristine $g-C_3N_4$ (Figure 12c,d).[56] The ESR results suggest that •O_2^- and •OH radical species could be generated by both $g-C_3N_4$ and AGCN-4 composites under visible light irradiation, and more •O_2^- and •OH radical species were generated in an AGCN-4-based reaction system. Moreover, to further analyze
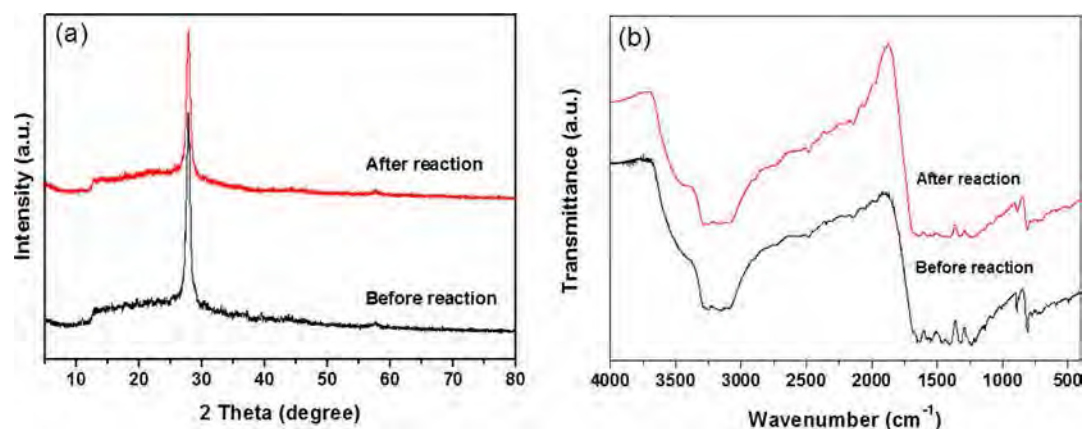
Figure 10. (a) XRD pattern and (b) FTIR spectra of the prepared AGCN-4 before and after the photocatalytic degradation process.
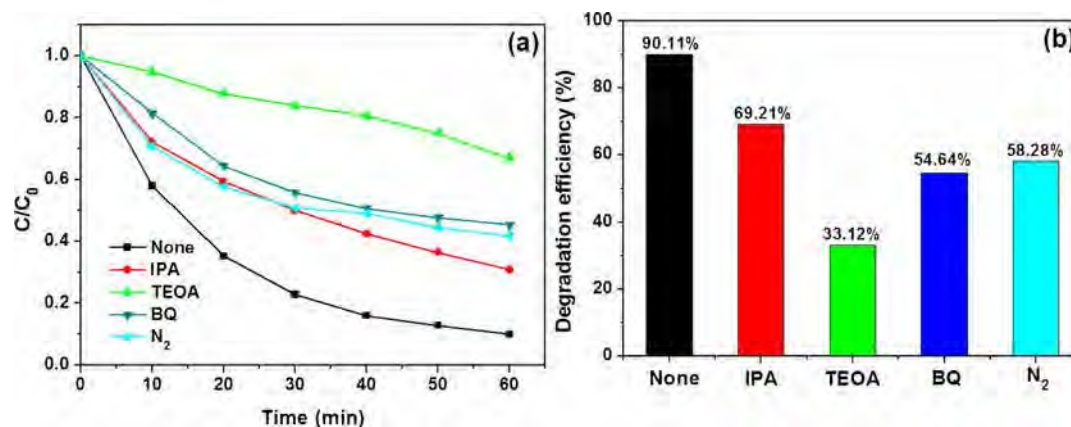

Figure 11. (a,b) Active radical species-trapping experiments for the photocatalytic degradation of TC and the corresponding photocatalytic removal efficiency over AGCN-4 nanocomposites under visible light irradiation.

the radical species production of the prepared samples under NIR irradiation, the ESR spin-trap experiments under NIR light irradiation have also been conducted. As shown in Figure S5, it can be seen that the prepared AGCN-4 also presents the characteristic peaks of $\bullet O_2^-$ and $\bullet OH$ species, which indicate the production of $\bullet O_2^-$ and $\bullet OH$ species under NIR light irradiation. However, under a similar condition, the characteristic peaks of $\bullet O_2^-$ and $\bullet OH$ species nearly cannot be observed, which indicates the very little production of these two radical species, and the results agree with the photocatalytic degradation results.

Therefore, on the basis of these experimental results, the reaction mechanism of the prepared Ag/N-GQDs/g-C$_3$N$_4$ nanocomposites is proposed and illustrated in Figure 13. N-GQDs, Ag NPs, and synergistic effects among all the components play multiple important roles in the system. The enhanced photocatalytic activity and removal efficiency are mainly attributed to the following two aspects: (1) enhanced light absorption and transformation effect and (2) accelerated photoexcited charge transportation and migration effect. In detail, under sunlight irradiation, g-C$_3$N$_4$ can only absorb the UV and visible light with wavelengths less than 460 nm and generate photoexcited electrons and holes. In the Ag/N-GQDs/g-C$_3$N$_4$ nanocomposites, the light with wavelengths longer than 460 nm can be efficiently utilized via the positive effect brought by N-GQDs and Ag NPs. Therefore, similar to the light with the wavelengths shorter than 550 nm, the Ag NPs have become the main contributor for their absorption because

the LSPR effect caused hot electrons, induced strong local electromagnetic fields, and thus increased the generated quantity of photo-excited electron−hole pairs. Simultaneously, similar to the catalysis under light with longer wavelengths ($\lambda >$ 550 nm), the role of N-GQDs would be the dominant. Owing to the upconversion effect of N-GQDs, the longer wavelengths can be upconverted to shorter wavelengths and subsequently absorbed by the Ag/g-C$_3$N$_4$ system to generate photoinduced charges. Meanwhile, the LSPR effect of Ag NPs can result in more visible light absorption, which further promotes the light-harvesting capacity of N-GQDs. Therefore, N-GQDs and Ag NPs can bring about an enhanced effect in Ag/N-GQDs/g-C$_3$N$_4$ nanocomposites, leading to the absorption, conversion, and enhancement effect of solar light utilization. Then, more photoinduced electron−holes pairs would be generated, the photoinduced electrons in the conduction band of g-C$_3$N$_4$ will be available to react with dissolved oxygen to generate superoxide oxygen radical species or further react with water for the formation of hydroxyl radical species and act on the degradation of TC. The photoinduced holes remained in the valence band of g-C$_3$N$_4$ can react with TC directly and contribute in its decomposition. Additionally, owing to the match band alignment, the N-GQDs and Ag NPs can be treated as electron sinks and reservoirs, facilitating efficient extraction of electrons from the conduction band of g-C$_3$N$_4$ and impeding the recombination of photogenerated charges. Therefore, in this system, both the LSPR effect of Ag NPs or the formed Mott−Schottky junction between Ag NPs and g-
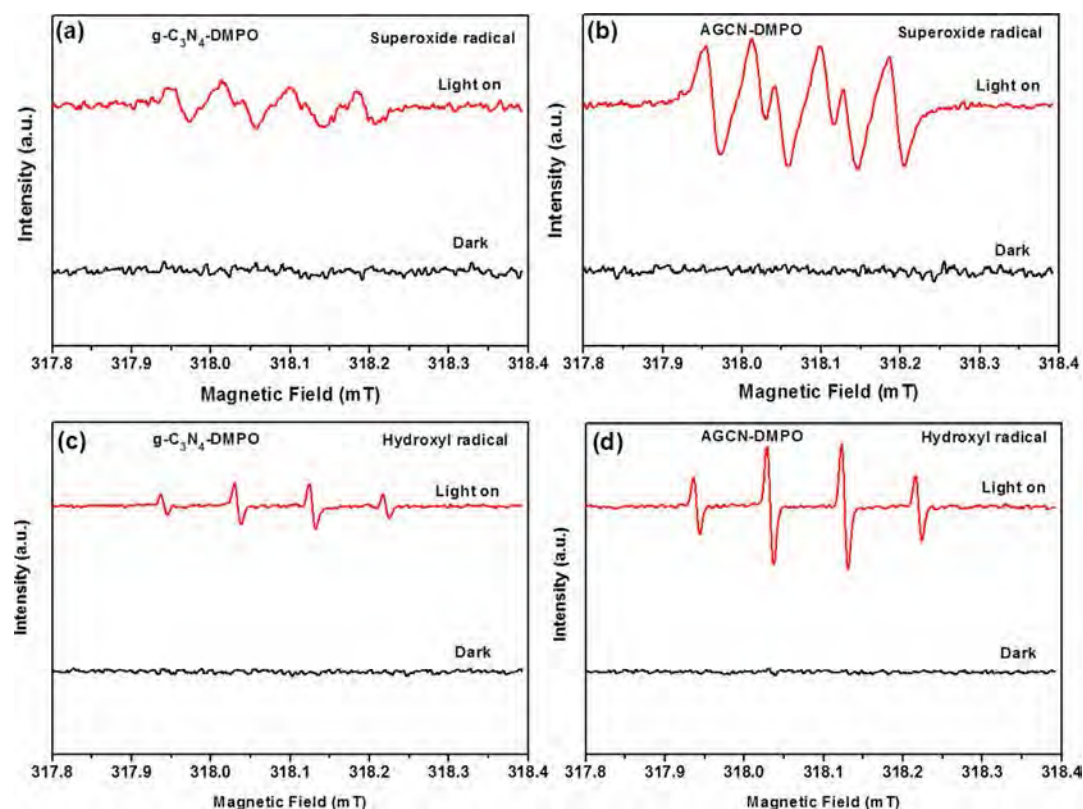
Figure 12. ESR spectra of radical adducts trapped by DMPO: (a,b) superoxide radical ($\bullet O_2^-$) for g-C_3N_4 and AGCN-4 nanocomposites and (c,d) hydroxyl radical ($\bullet OH$) in g-C_3N_4 and AGCN-4 nanocomposites in the dark and with the visible light irradiation for 10 min.
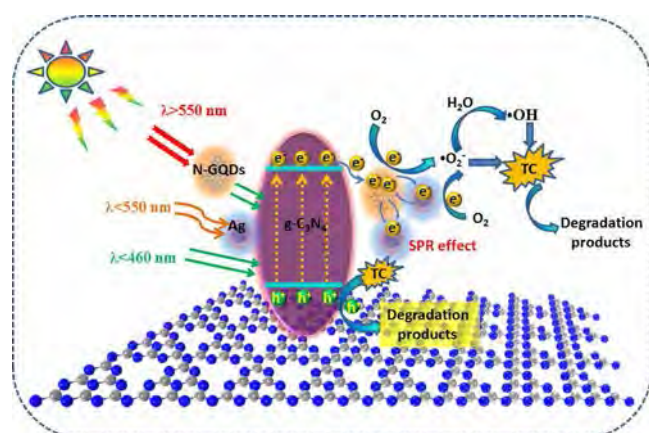

Figure 13. Schematic illustration of the proposed photocatalytic reaction mechanism and photogenerated charge transfer pathway over Ag/N-GQDs/g-C_3N_4 nanocomposites toward TC degradation under full-spectrum light irradiation.

C_3N_4 would promote the transfer rate of photogenerated electrons and holes, inhibiting the recombination rate; N-GQDs own the electron transfer properties, promoting the charge separation and transportation; the synergistic effect between N-GQDs and Ag NPs can further facilitate efficient extraction of electrons from the conduction band of g-C_3N_4 and impeding the recombination of photogenerated charges. In short, the synergistic effects among g-C_3N_4, N-GQDs, and Ag NPs contribute to the improvement of photocatalytic activity and degradation performance in full-spectrum solar light.

4. CONCLUSIONS

In summary, a novel Ag/N-GQDs/g-C_3N_4 nanocomposite with full-spectrum light response ability has been successfully prepared via a simple process. The contents of both N-GQDs and Ag NPs show great influence on the photocatalytic activity of the hybrid nanocomposites, and the optimum Ag/N-GQDs/g-C_3N_4 (with the content of 0.5% N-GQDs and 2.0% Ag NPs) presents a 92.8, 90.11, and 31.3% for TC removal under light irradiation with the wavelengths larger than 365, 420, and 760 nm, respectively, indicating that the prepared Ag/N-GQDs/g-C_3N_4 presents boosted photocatalytic performance not only in visible light but also in the full spectrum and even in NIR light. It is the headmost report that the combination of the LSPR effect from Ag NPs with the upconverted effect of N-GQDs was integrated with g-C_3N_4 for the utilization of broad-spectrum light. The enhanced photocatalytic activity can be attributed to the enhanced effect of N-GQDs and Ag NPs. The combination of the LSPR effect from Ag NPs with the upconverted effect of N-GQDs results in the enhanced light transfer and absorption ability of the Ag/N-GQDs/g-C_3N_4 nanocomposites, which results in quantities of photogenerated charges. Moreover, the intimate contact of Ag NPs, N-GQDs, and g-C_3N_4 benefits the transfer of the photogenerated charges, inhibiting the recombination efficiency, and more photogenerated charges can participate in the degradation process. Herein, the novel Ag/N-GQDs/g-C_3N_4 nanocomposites can provide efficient strategies for the design of highly efficient broad-spectrum response photocatalysts.

ASSOCIATED CONTENT

Supporting Information

The Supporting Information is available free of charge on the ACS Publications website at DOI: 10.1021/acsami.7b14541.

Spectral profile of the irradiation source, photographs of the photocatalytic reaction system, photocatalytic process of the prepared of N-GQDs and Ag nanoparticle-coated g-C_3N_4 nanocomposites and corresponding reaction dynamic data, upconverted photoluminescence spectra of the prepared N-GQDs, ESR spectra of the prepared g-C_3N_4 and AGCN-4 samples under NIR light irradiation, and the element content of the prepared g-C_3N_4, GCN-3, and AGCN-4 (PDF)

AUTHOR INFORMATION

Corresponding Authors

*E-mail: tanglin@hnu.edu.cn. Phone: +86-731-88822778. Fax: +86-731-88823701 (L.T.).
*E-mail: zgming@hnu.edu.cn (G.Z.).

ORCID

Lin Tang: 0000-0001-6996-7955
Guangming Zeng: 0000-0002-4230-7647

Notes

The authors declare no competing financial interest.

ACKNOWLEDGMENTS

REFERENCES

(1) Qu, Y.; Duan, X. Progress, challenge and perspective of heterogeneous photocatalysts. Chem. Soc. Rev. 2013, 42, 2568−2580.

(2) Zhou, P.; Yu, J.; Jaroniec, M. All-solid-state Z-scheme photocatalytic systems. Adv. Mater. 2014, 26, 4920−4935.

(3) Lee, J. S.; You, K. H.; Park, C. B. Highly photoactive, low bandgap TiO_2 nanoparticles wrapped by graphene. Adv. Mater. 2012, 24, 1084−1088.

(4) Wang, W.; Huang, X.; Wu, S.; Zhou, Y.; Wang, L.; Shi, H.; Liang, Y.; Zou, B. Preparation of p−n junction Cu_2O/$BiVO_4$ heterogeneous nanostructures with enhanced visible-light photocatalytic activity. Appl. Catal., B 2013, 134−135, 293−301.

(5) Zhou, B.; Zhao, X.; Liu, H.; Qu, J.; Huang, C. P. Visible-light sensitive cobalt-doped $BiVO_4$ (Co-$BiVO_4$) photocatalytic composites for the degradation of methylene blue dye in dilute aqueous solutions. Appl. Catal., B 2010, 99, 214−221.

(6) Kong, H. J.; Won, D. H.; Kim, J.; Woo, S. I. Sulfur-Doped g-C_3N_4/$BiVO_4$ Composite Photocatalyst for Water Oxidation under Visible Light. Chem. Mater. 2016, 28, 1318−1324.

(7) Li, W.; Feng, C.; Dai, S.; Yue, J.; Hua, F.; Hou, H. Fabrication of sulfur-doped g-C_3N_4/Au/CdS Z-scheme photocatalyst to improve the photocatalytic performance under visible light. Appl. Catal., B 2015, 168−169, 465−471.

(8) Wang, J.; Tang, L.; Zeng, G.; Liu, Y.; Zhou, Y.; Deng, Y.; Wang, J.; Peng, B. Plasmonic Bi Metal Deposition and g-C_3N_4 coating on Bi_2WO_6 Microspheres for Efficient Visible-Light Photocatalysis. ACS Sustainable Chem. Eng. 2017, 5, 1062−1072.

(9) Wang, J.; Tang, L.; Zeng, G.; Deng, Y.; Liu, Y.; Wang, L.; Zhou, Y.; Guo, Z.; Wang, J.; Zhang, C. Atomic scale g-C_3N_4/Bi_2WO_6 2D/2D heterojunction with enhanced photocatalytic degradation of ibuprofen under visible light irradiation. Appl. Catal., B 2017, 209, 285−294.

(10) Tang, L.; Wang, J.; Zeng, G.; Liu, Y.; Deng, Y.; Zhou, Y.; Tang, J.; Wang, J.; Guo, Z. Enhanced photocatalytic degradation of norfloxacin in aqueous Bi_2WO_6 dispersions containing nonionic surfactant under visible light irradiation. J. Hazard. Mater. 2016, 306, 295−304.

(11) Wang, X.; Chen, X.; Thomas, A.; Fu, X.; Antonietti, M. Metal-Containing Carbon Nitride Compounds: A New Functional Organic-Metal Hybrid Material. Adv. Mater. 2009, 21, 1609−1612.

(12) Li, H.; Liu, Y.; Cui, Y.; Zhang, W.; Fu, C.; Wang, X. Facile synthesis and enhanced visible-light photoactivity of $DyVO_4$/g-C_3N_4 composite semiconductors. Appl. Catal., B 2016, 183, 426−432.

(13) Deng, Y.; Tang, L.; Zeng, G.; Zhu, Z.; Yan, M.; Zhou, Y.; Wang, J.; Liu, Y.; Wang, J. Insight into highly efficient simultaneous photocatalytic removal of Cr(VI) and 2,4-diclorophenol under visible light irradiation by phosphorus doped porous ultrathin g-C_3N_4 nanosheets from aqueous media: Performance and reaction mechanism. Appl. Catal., B 2017, 203, 343−354.

(14) Deng, Y.; Tang, L.; Zeng, G.; Wang, J.; Zhou, Y.; Wang, J.; Tang, J.; Liu, Y.; Peng, B.; Chen, F. Facile fabrication of a direct Z-scheme Ag_2CrO_4/g-C_3N_4 photocatalyst with enhanced visible light photocatalytic activity. J. Mol. Catal. A: Chem. 2016, 421, 209−221.

(15) Zhang, M.; Luo, W.; Wei, Z.; Jiang, W.; Liu, D.; Zhu, Y. Separation free C_3N_4/SiO_2 hybrid hydrogels as high active photocatalysts for TOC removal. Appl. Catal., B 2016, 194, 105−110.

(16) Yan, M.; Zhu, F.; Gu, W.; Sun, L.; Shi, W.; Hua, Y. Construction of nitrogen-doped graphene quantum dots-$BiVO_4$/g-C_3N_4 Z-scheme photocatalyst and enhanced photocatalytic degradation of antibiotics under visible light. RSC Adv. 2016, 6, 61162−61174.

(17) Muñoz-Batista, M. J.; Fernández-García, M.; Kubacka, A. Promotion of CeO_2−TiO_2 photoactivity by g-C_3N_4: Ultraviolet and visible light elimination of toluene. Appl. Catal., B 2015, 164, 261−270.

(18) Fontelles-Carceller, O.; Muñoz-Batista, M. J.; Fernández-García, M.; Kubacka, A. Interface Effects in Sunlight-Driven Ag/g-C_3N_4 Composite Catalysts: Study of the Toluene Photodegradation Quantum Efficiency. ACS Appl. Mater. Interfaces 2016, 8, 2617−2627.

(19) Li, Y.; Li, K.; Yang, Y.; Li, L.; Xing, Y.; Song, S.; Jin, R.; Li, M. Ultrathin g-C_3N_4 Nanosheets Coupled with $AgIO_3$ as Highly Efficient Heterostructured Photocatalysts for Enhanced Visible-Light Photocatalytic Activity. Chem.—Eur. J. 2015, 21, 17739−17747.

(20) Zhang, M.; Jiang, W.; Liu, D.; Wang, J.; Liu, Y.; Zhu, Y.; Zhu, Y. Photodegradation of phenol via C_3N_4-agar hybrid hydrogel 3D photocatalysts with free separation. Appl. Catal., B 2016, 183, 263−268.

(21) Shi, Y.; Yang, Z.; Liu, Y.; Yu, J.; Wang, F.; Tong, J.; Su, B.; Wang, Q. Fabricating a g-C_3N_4/CuOx heterostructure with tunable valence transition for enhanced photocatalytic activity. RSC Adv. 2016, 6, 39774−39783.

(22) Zhang, H.; Zhao, L.; Geng, F.; Guo, L.-H.; Wan, B.; Yang, Y. Carbon dots decorated graphitic carbon nitride as an efficient metal-free photocatalyst for phenol degradation. Appl. Catal., B 2016, 180, 656−662.

(23) Liu, Q.; Chen, T.; Guo, Y.; Zhang, Z.; Fang, X. Ultrathin g-C_3N_4 nanosheets coupled with carbon nanodots as 2D/0D composites for efficient photocatalytic H_2 evolution. Appl. Catal., B 2016, 193, 248−258.

(24) Deng, Y.; Tang, L.; Zeng, G.; Feng, C.; Dong, H.; Wang, J.; Feng, H.; Liu, Y.; Zhou, Y.; Pang, Y. Plasmonic resonance excited dual Z-scheme $BiVO_4$/Ag/Cu_2O nanocomposite: synthesis and mechanism for enhanced photocatalytic performance in recalcitrant antibiotic degradation. Environ. Sci.: Nano 2017, 4, 1494−1511.

(25) Xu, C.; Han, Q.; Zhao, Y.; Wang, L.; Li, Y.; Qu, L. Sulfur-doped graphitic carbon nitride decorated with graphene quantum dots for an efficient metal-free electrocatalyst. J. Mater. Chem. A 2015, 3, 1841−1846.

(26) Zou, J.-P.; Wang, L.-C.; Luo, J.; Nie, Y.-C.; Xing, Q.-J.; Luo, X.-B.; Du, H.-M.; Luo, S.-L.; Suib, S. L. Synthesis and efficient visible light

photocatalytic H_2 evolution of a metal-free g-C_3N_4/graphene quantum dots hybrid photocatalyst. *Appl. Catal., B* **2016**, *193*, 103−109.

(27) Pan, D.; Zhang, J.; Li, Z.; Wu, M. Hydrothermal route for cutting graphene sheets into blue-luminescent graphene quantum dots. *Adv. Mater.* **2010**, *22*, 734−738.

(28) Yin, Y.; Liu, Q.; Jiang, D.; Du, X.; Qian, J.; Mao, H.; Wang, K. Atmospheric pressure synthesis of nitrogen doped graphene quantum dots for fabrication of BiOBr nanohybrids with enhanced visible-light photoactivity and photostability. *Carbon* **2016**, *96*, 1157−1165.

(29) Tang, L.; Ji, R.; Li, X.; Teng, K. S.; Lau, S. P. Energy-level structure of nitrogen-doped graphene quantum dots. *J. Mater. Chem. C* **2013**, *1*, 4908.

(30) Li, Y.; Zhao, Y.; Cheng, H.; Hu, Y.; Shi, G.; Dai, L.; Qu, L. Nitrogen-doped graphene quantum dots with oxygen-rich functional groups. *J. Am. Chem. Soc.* **2012**, *134*, 15−18.

(31) Zhu, Z.; Lu, Z.; Wang, D.; Tang, X.; Yan, Y.; Shi, W.; Wang, Y.; Gao, N.; Yao, X.; Dong, H. Construction of high-dispersed Ag/Fe$_3$O$_4$/g-C_3N_4 photocatalyst by selective photo-deposition and improved photocatalytic activity. *Appl. Catal., B* **2016**, *182*, 115−122.

(32) Sinatra, L.; LaGrow, A. P.; Peng, W.; Kirmani, A. R.; Amassian, A.; Idriss, H.; Bakr, O. M. A Au/Cu$_2$O−TiO$_2$ system for photocatalytic hydrogen production. A pn-junction effect or a simple case of in situ reduction? *J. Catal.* **2015**, *322*, 109−117.

(33) Jing, L.; Xu, Y.; Huang, S.; Xie, M.; He, M.; Xu, H.; Li, H.; Zhang, Q. Novel magnetic CoFe$_2$O$_4$/Ag/Ag$_3$VO$_4$ composites: Highly efficient visible light photocatalytic and antibacterial activity. *Appl. Catal., B* **2016**, *199*, 11−22.

(34) Xu, D.; Chen, M.; Song, S.; Jiang, D.; Fan, W.; Shi, W. The synthesis of a novel Ag−NaTaO$_3$ hybrid with plasmonic photocatalytic activity under visible-light. *CrystEngComm* **2014**, *16*, 1384.

(35) Bing, W.; Chen, Z.; Sun, H.; Shi, P.; Gao, N.; Ren, J.; Qu, X. Visible-light-driven enhanced antibacterial and biofilm elimination activity of graphitic carbon nitride by embedded Ag nanoparticles. *Nano Res.* **2015**, *8*, 1648−1658.

(36) Yang, Y.; Guo, Y.; Liu, F.; Yuan, X.; Guo, Y.; Zhang, S.; Guo, W.; Huo, M. Preparation and enhanced visible-light photocatalytic activity of silver deposited graphitic carbon nitride plasmonic photocatalyst. *Appl. Catal., B* **2013**, *142−143*, 828−837.

(37) Tian, K.; Liu, W.-J.; Jiang, H. Comparative Investigation on Photoreactivity and Mechanism of Biogenic and Chemosythetic Ag/C$_3$N$_4$ Composites under Visible Light Irradiation. *ACS Sustainable Chem. Eng.* **2015**, *3*, 269−276.

(38) Ma, S.; Zhan, S.; Jia, Y.; Shi, Q.; Zhou, Q. Enhanced disinfection application of Ag-modified g-C_3N_4 composite under visible light. *Appl. Catal., B* **2016**, *186*, 77−87.

(39) Niu, P.; Zhang, L.; Liu, G.; Cheng, H.-M. Graphene-Like Carbon Nitride Nanosheets for Improved Photocatalytic Activities. *Adv. Funct. Mater.* **2012**, *22*, 4763−4770.

(40) Liu, J.; Xu, H.; Xu, Y.; Song, Y.; Lian, J.; Zhao, Y.; Wang, L.; Huang, L.; Ji, H.; Li, H. Graphene quantum dots modified mesoporous graphite carbon nitride with significant enhancement of photocatalytic activity. *Appl. Catal., B* **2017**, *207*, 429−437.

(41) Qin, J.; Zeng, H. Photocatalysts fabricated by depositing plasmonic Ag nanoparticles on carbon quantum dots/graphitic carbon nitride for broad spectrum photocatalytic hydrogen generation. *Appl. Catal., B* **2017**, *209*, 161−173.

(42) Xin, X.; Lang, J.; Wang, T.; Su, Y.; Zhao, Y.; Wang, X. Construction of novel ternary component photocatalyst Sr$_{0.25}$H$_{1.5}$Ta$_2$O$_6$·H$_2$O coupled with g-C_3N_4 and Ag toward efficient visible light photocatalytic activity for environmental remediation. *Appl. Catal., B* **2016**, *181*, 197−209.

(43) Ran, J.; Ma, T. Y.; Gao, G.; Du, X.-W.; Qiao, S. Z. Porous P-doped graphitic carbon nitride nanosheets for synergistically enhanced visible-light photocatalytic H_2 production. *Energy Environ. Sci.* **2015**, *8*, 3708−3717.

(44) She, X.; Xu, H.; Xu, Y.; Yan, J.; Xia, J.; Xu, L.; Song, Y.; Jiang, Y.; Zhang, Q.; Li, H. Exfoliated graphene-like carbon nitride in organic solvents: enhanced photocatalytic activity and highly selective and

sensitive sensor for the detection of trace amounts of Cu^{2+}. *J. Mater. Chem. A* **2014**, *2*, 2563.

(45) Xu, J.; Zhang, L.; Shi, R.; Zhu, Y. Chemical exfoliation of graphitic carbon nitride for efficient heterogeneous photocatalysis. *J. Mater. Chem. A* **2013**, *1*, 14766.

(46) Lin, Z.; Wang, X. Nanostructure Engineering and Doping of Conjugated Carbon Nitride Semiconductors for Hydrogen Photosynthesis. *Angew. Chem., Int. Ed.* **2013**, *52*, 1735−1738.

(47) Yang, Z.; Xu, M.; Liu, Y.; He, F.; Gao, F.; Su, Y.; Wei, H.; Zhang, Y. Nitrogen-doped, carbon-rich, highly photoluminescent carbon dots from ammonium citrate. *Nanoscale* **2014**, *6*, 1890−1895.

(48) Liu, S.; Tian, J.; Wang, L.; Zhang, Y.; Qin, X.; Luo, Y.; Asiri, A. M.; Al-Youbi, A. O.; Sun, X. Hydrothermal treatment of grass: a low-cost, green route to nitrogen-doped, carbon-rich, photoluminescent polymer nanodots as an effective fluorescent sensing platform for label-free detection of Cu(II) ions. *Adv. Mater.* **2012**, *24*, 2037−2041.

(49) Zhao, W.; Guo, Y.; Faiz, Y.; Yuan, W.-T.; Sun, C.; Wang, S.-M.; Deng, Y.-H.; Zhuang, Y.; Li, Y.; Wang, X.-M.; He, H.; Yang, S.-G. Facile in-suit synthesis of Ag/AgVO$_3$ one-dimensional hybrid nanoribbons with enhanced performance of plasmonic visible-light photocatalysis. *Appl. Catal., B* **2015**, *163*, 288−297.

(50) Xiong, J.; Li, Z.; Chen, J.; Zhang, S.; Wang, L.; Dou, S. Facile synthesis of highly efficient one-dimensional plasmonic photocatalysts through Ag@Cu$_2$O core-shell heterononowires. *ACS Appl. Mater. Interfaces* **2014**, *6*, 15716−15725.

(51) Qu, D.; Zheng, M.; Zhang, L.; Zhao, H.; Xie, Z.; Jing, X.; Haddad, R. E.; Fan, H.; Sun, Z. Formation mechanism and optimization of highly luminescent N-doped graphene quantum dots. *Sci. Rep.* **2014**, *4*, 5294.

(52) Wang, L.; Wang, Y.; Xu, T.; Liao, H.; Yao, C.; Liu, Y.; Li, Z.; Chen, Z.; Pan, D.; Sun, L.; Wu, M. Gram-scale synthesis of single-crystalline graphene quantum dots with superior optical properties. *Nat. Commun.* **2014**, *5*, 5357.

(53) Linic, S.; Christopher, P.; Ingram, D. B. Plasmonic-metal nanostructures for efficient conversion of solar to chemical energy. *Nat. Mater.* **2011**, *10*, 911−921.

(54) Wei, X.; Shao, C.; Li, X.; Lu, N.; Wang, K.; Zhang, Z.; Liu, Y. Facile in situ synthesis of plasmonic nanoparticles-decorated g-C_3N_4/TiO$_2$ heterojunction nanofibers and comparison study of their photosynergistic effects for efficient photocatalytic H_2 evolution. *Nanoscale* **2016**, *8*, 11034−11043.

(55) Deng, Y.; Tang, L.; Zeng, G.; Dong, H.; Yan, M.; Wang, J.; Hu, W.; Wang, J.; Zhou, Y.; Tang, J. Enhanced visible light photocatalytic performance of polyaniline modified mesoporous single crystal TiO$_2$ microsphere. *Appl. Surf. Sci.* **2016**, *387*, 882−893.

(56) Muñoz-Batista, M. J.; Fontelles-Carceller, O.; Ferrer, M.; Fernández-García, M.; Kubacka, A. Disinfection capability of Ag/g-C_3N_4 composite photocatalysts under UV and visible light illumination. *Appl. Catal., B* **2016**, *183*, 86−95.